

Nitrogen isotope fractionation during magma ocean degassing: tracing the composition of early Earth's atmosphere

C. Dalou, C. Deligny, E. Füre

Supplementary Information

The Supplementary Information includes:

- 1. Methods
- 2. Supplementary Discussion
- Tables S-1 and S-2
- Figures S-1 to S-3
- Supplementary Information References

1. Methods

Synthesis of starting material

Two series of mafic glasses were prepared:

- a series of Fe-free glasses, noted PB, for the degassing experiments presented in the main text was designed to equilibrate magma-ocean-like melts with a N-rich gas; and to avoid N partitioning into Fe metal blobs at low fO_2 conditions (Dalou *et al.*, 2017; Speelmanns *et al.*, 2019; Grewal *et al.*, 2019).
- a series of Fe-bearing glasses, noted PBF, was designed to equilibrate magma-ocean-like melts and a Fe-N or Fe-Si-N alloy (\pm N-rich gas) under reducing conditions to allow the calculation of fO_2 conditions.

These mafic glasses were synthesised based on the magma ocean composition proposed by Fichtner *et al.* (2021). The starting composition was chosen to account for MgO dissolution from the forsterite capsule at 1550 °C, which here increased the MgO concentration of the melt from 9.7 to up to 22 wt. % (Table S-1). Using this composition, we obtained well-quenched MgO-rich glasses that were relatively depolymerised (*i.e.* NBO/T \geq 1, where NBO/T is the ratio of non-bridging oxygens to tetrahedral cations).

The starting powders were prepared by mixing pre-dried, spectroscopically pure SiO₂, Al₂O₃, MgO, CaCO₃, Na₂CO₃, and K₂CO₃ reagents. The mixtures were decarbonated by slow heating (3 °C/min), then fused in air for 2 h at 1350 °C in platinum crucibles in a 1 atm furnace. Melts were quenched to glass in water, then crushed and hand ground



in an agate mortar for 45 min. After decarbonating the glass powders, Fe was added to the PBF series as FeO powder, whereas the PB series remained Fe free. Nitrogen was added to both series using 0.5–8 wt. % Si_3N_4 , noted ‘0.5N’ to ‘8N’ in the sample names. Both $\text{Si}_3^{14}\text{N}_4$ and $\text{Si}_3^{15}\text{N}_4$ powders (prepared as described in Dalou *et al.*, 2019) were used to yield an initial $^{15}\text{N}/^{14}\text{N}$ ratio of 0.946 ± 0.003 . By varying the amount of Si_3N_4 added to the starting compositions and adding additional Si powder (2, 3 and 6 wt. %, noted ‘2Si’, ‘3Si’, and ‘6Si’ in the sample names), we were able to change (but not control) the sample $f\text{O}_2$ because Si_3N_4 and Si have a strong reducing effect (Dalou *et al.*, 2017). The starting materials were loaded into pure forsterite capsules to ensure reducing conditions and prevent N loss. Glasses were originally anhydrous but were likely contaminated by atmospheric hydrogen, since N-H vibrations were observed in the experimental run products.

Experimental procedure

Experiments were performed in a 1/2-inch piston cylinder at 1.5 GPa and 1550 °C at the Centre de Recherches Pétrographiques et Géochimiques (CRPG, Nancy, France). Run temperatures were controlled to within ~ 1 °C of the set point using $\text{W}_{95}\text{Re}_5/\text{W}_{74}\text{Re}_{26}$ thermocouples. The duration of the experiments was 6 h, which is sufficient to reach compositional equilibrium (Dalou *et al.*, 2017). Before decompression, the power to the furnace was cut and the experiment was quenched rapidly (~ 175 °C/s). During this stage of decompression, the forsterite capsules suffered cracking, which divided them into three to six lamellae 0.2–0.8 mm thick.

Hence, the final run product from each experiment consisted of various lamellae of glass embedded in forsterite, which were individually mounted in epoxy and polished with ethanol. For each experiment, the best sample was selected: the sample with the largest bubbles was selected for Raman spectroscopy (PB series) and that with the largest metal blobs for electron probe microanalysis (EPMA, all glasses). The selected lamellae were then removed from the resin, pressed into high-purity indium metal mounts, and gold coated for SIMS analysis. After re-polishing to remove any coating to avoid interference from Au vibrational bands, mounts from the PB series were analysed by Raman spectroscopy, and then all glasses were carbon coated for EPMA.

SIMS analyses

In-situ SIMS analyses of N concentrations and isotopic ratios in the silicate glasses were performed at the CRPG using the CAMECA 1280-HR2. Nitrogen ($^{14}\text{N} + ^{15}\text{N}$) contents and isotopic ratios (Table 1) were measured by analysing the secondary molecular ions $^{14}\text{N}^{16}\text{O}^-$ and $^{15}\text{N}^{16}\text{O}^-$ at masses 30 and 31, respectively, at a nominal mass resolution of 14,000. A 10 kV Cs^+ primary ion beam was used with a ~ 10 nA current, resulting in a beam diameter of 15–20 μm , and a normal-incidence electron gun was used for charge compensation. To minimise surface contamination, glass surfaces were pre-sputtered for 180 s over a 10×10 μm area prior to signal acquisition. Further details on the SIMS N analysis procedure are available in Füre *et al.* (2018). The $^{14}\text{N}^{16}\text{O}^-$ and $^{15}\text{N}^{16}\text{O}^-$ ions were measured for 30 cycles in peak-jumping mode on an electron multiplier for 6 s, together with $^{27}\text{Al}^-$ (3 s), $^{30}\text{Si}^-$ (3 s), and $^{16}\text{O}_2^-$ (3 s) on a faraday cup. We used a suite of eight reference glasses with known N concentrations and isotopic compositions to determine the N contents in



the silicate glasses based on the $^{14}\text{N}^{16}\text{O}^-$ count rate normalised by the $^{16}\text{O}_2^-$ signal (Füri *et al.*, 2018). This method has been shown to yield N contents in excellent agreement with static mass spectrometry analyses for glasses of variable composition and containing ≤ 1 to 6,000 ppm N (Boulliung *et al.*, 2020). Based on repeated isotopic ratio measurements of five reference glasses containing ≥ 136 ppm N ($\delta^{15}\text{N}_{\text{true}} = -4 \pm 1 \text{ ‰}$), the instrumental mass fractionation (IMF) for glass analyses was determined to be $\alpha_{\text{inst}} = 1.0120 \pm 0.0015$ (2σ ; Fig. S-1). Thus, the measured $^{15}\text{N}/^{14}\text{N}$ ratios of the experimental glasses were corrected for IMF as $(^{15}\text{N}/^{14}\text{N})_{\text{corr}} = (^{15}\text{N}/^{14}\text{N})_{\text{measured}} / \alpha_{\text{inst}}$.

Raman spectroscopy analyses

Raman spectroscopy was performed using a LabRAM HR microspectrometer (Horiba Jobin Yvon) at GeoRessources (Nancy, France) using the 457.9 nm radiations of an Ar^+ laser (Stabilite 2017, Spectra-Physics) with 154 mW output. The laser intensity was focused to a $\sim 2 \mu\text{m}$ spot-size with 7 mW on-sample through a $50\times$ long-working-distance Olympus objective with a 0.5 numerical aperture. The spectrometer was equipped with a 1,800 grooves/mm grating. Acquisition times were 10 s, with 20 acquisitions collected per spectrum. To observe Si-N vibrations, molecular N_2 vibrations, and N-H vibrations in the degassed silicate glasses, spectra were acquired in the 700–1200, 2000–2400, and 3060–3560 cm^{-1} spectral windows, respectively. No baseline corrections were applied to the spectra presented in Figure 3.

To analyse gas bubble contents, the laser was focused into the largest bubbles ($>30 \mu\text{m}$ in diameter) and spectra were acquired for 15 s with 30 acquisitions, centred on the 2200 and 3160 cm^{-1} spectral windows. In these bubbles, the N triple bond vibration of molecular N_2 , and the C-H vibration in CH_4 were observed at 2331 and 2917 cm^{-1} , respectively (Fig. S-2). We note the absence of N-H vibrations in the range 3200–3450 cm^{-1} .

EPMA

Major element compositions of glasses and metal blobs (in Fe-bearing samples) were determined using a CAMECA SXFive-Tactics at the Laboratoire Magmas et Volcans (Clermont-Ferrand, France). For glass analyses, we used an accelerating voltage of 15 kV and a 8 nA beam defocused to 10 μm . Wollastonite (Si, Ca), basaltic glass VG2 (Al), Fe_2O_3 (Fe), MgO (Mg), and albite (Na) were used as standards. For metal alloys, we used a 15 kV accelerating voltage and a 15 nA focused beam. Along with Fe, the Pt and Si concentrations in the metal phases of all samples were measured, and pure Fe, Si, and Pt were used as metal standards. Aluminium was analysed to check for silicate contamination during metal analyses, using VG2 as a standard. The major element compositions of silicate glasses determined by EPMA are presented in Table S-1 and those of metal blobs in Table S-2.



Oxygen fugacity calculation

Oxygen fugacities, expressed as $\log f_{\text{O}_2}$ (IW), were estimated from the equilibrium reaction $\text{FeO}_{\text{silicate melt}} = \text{Fe}_{\text{liquid metal}} + 1/2 \text{O}_2$ for Fe-bearing samples. Following this equilibrium, f_{O_2} was calculated using the relationship between the mole fractions of FeO in silicate melt ($X_{\text{FeO}}^{\text{melt}}$) and Fe in liquid metal ($X_{\text{Fe}}^{\text{alloy}}$), their associated activity coefficients ($\gamma_{\text{FeO}}^{\text{melt}}$ and $\gamma_{\text{Fe}}^{\text{alloy}}$, respectively), and the equilibrium constant (K) of the reaction (Médard *et al.*, 2008) as described in Dalou *et al.* (2017):

$$\log_{10} f_{\text{O}_2} = \frac{2}{\ln(10)} \left[\ln \left(\frac{X_{\text{FeO}}^{\text{melt}}}{X_{\text{Fe}}^{\text{alloy}}} \right) - \ln \left(\gamma_{\text{Fe}}^{\text{alloy}} \right) + \ln \left(\gamma_{\text{FeO}}^{\text{melt}} \right) - \ln K \right] \quad \text{Eq. S-1}$$

$\gamma_{\text{Fe}}^{\text{alloy}}$ was derived via the MetalAct metal activity calculator (Wade and Wood, 2005) for each sample and $\gamma_{\text{FeO}}^{\text{melt}}$ was assumed to be 1.2 (Dalou *et al.*, 2017, 2019). We used the method of Stanley *et al.* (2014) and Zhang *et al.* (2016) to directly compare the resulting f_{O_2} to the IW buffer, which is referenced to solid Fe metal. The f_{O_2} conditions of the PBF series could only be determined in 5 samples (Fig. S-3a and Table S-2), in which the metal blobs were $>5 \mu\text{m}$ in diameter (Fig. S-3b); the f_{O_2} values of these samples range from IW -2.3 to IW -4.2 . The f_{O_2} conditions in samples PBF05N and PBF2N, in which metal blobs were too small to be analysed, were roughly estimated by extrapolation of the trend in Figure S-3a.

Because each PB sample has an equivalent PBF sample in terms of initial Si_3N_4 and Si metal concentrations (*e.g.*, PB4N2Si and PBF4N2Si), we assumed that the f_{O_2} determined for each PBF sample corresponds to that of its equivalent in the PB series. Although this is a very rough approximation (± 0.5 log units), this indirect method of estimating f_{O_2} in the degassed Fe-free glasses enabled us to discuss the effect of f_{O_2} conditions on N solubility in the main text.

$P(\text{N}_2)$ calculation

Determining the partial pressure of nitrogen $P(\text{N}_2)$ or nitrogen fugacity f_{N_2} in the gas phase (*i.e.*, bubbles) of the samples from this study could provide more quantitative information on the effect of the gas composition on the solubility and isotopic fractionation of N. Indeed, it could be used to calculate the equilibrium constant K of the different N degassing reactions. Bernadou *et al.* (2021) calculated $P(\text{N}_2)$ in the fluid phase of their experiments by quantifying the partial pressure of other species within the fluid phase: H_2O , CO_2 , CO, and H_2 . They determined the pressure of H_2O and CO_2 by converting the measured IR band intensities into concentrations following Shishkina *et al.* (2010), and then into partial pressures using the numerical model of Iacono-Marziano *et al.* (2012). The partial pressures of CO and H_2 were determined using the activities of C (graphite) and water and f_{O_2} by using the equilibrium reaction presented in Bernadou *et al.* (2021). They then calculated $P(\text{N}_2)$ by subtracting the fugacities of the other species from the “total



pressure” of the experiment and converted $P(\text{N}_2)$ to $f\text{N}_2$ by applying different coefficients depending on the pressure conditions of their experiments.

Unfortunately, we cannot apply this method to our experiments because only two bubbles in two experiments performed at the same pressure and temperature conditions were analysed by Raman spectroscopy. As previously mentioned, N_2 and CH_4 were detected in the bubbles by Raman spectroscopy, but, unlike IR band intensities, Raman band intensities cannot be converted into concentrations, which are necessary to follow the methods of [Bernadou *et al.* \(2021\)](#) or [Hirschmann *et al.* \(2012\)](#) for H_2 . Moreover, because N_2 is not the only gas species in the bubbles, its pressure cannot be considered as equivalent to the confining pressure. Even considering the mixed gases species in the bubbles, [Zhang and Duan \(2009\)](#) do not provide the equations of state to calculate the fugacities of N_2 and CH_4 at pressure conditions relevant to our study (>1 GPa). Therefore, calculating $P(\text{N}_2)$ in the samples from this study would require numerous assumptions and generate meaningless values.

2. Supplementary Discussion

H, C, and S isotopic variations observed during basaltic magma degassing

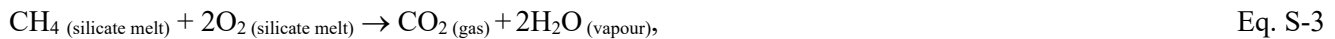
Studies of degassed basalts, whether terrestrial mid-ocean ridge basalts ([Pineau and Javoy, 1994](#); [Cartigny *et al.*, 2001](#)), ocean island basalts ([Gerlach and Taylor, 1990](#); [Aubaud *et al.*, 2006](#)), arc basalts ([De Hoog *et al.*, 2001](#); [Hauri, 2002](#)), or lunar basalts ([Saal and Hauri, 2021](#)) have shown H, C, and S isotopic variations consistent with our observations for N isotopes during degassing.

In natural degassed basaltic glasses, H and C become isotopically lighter with increased degassing (*e.g.*, [Taylor *et al.*, 1986](#); [Gerlach and Taylor, 1990](#); [Pineau and Javoy, 1994](#); [Cartigny *et al.*, 2001](#); [Hauri, 2002](#)). For instance, melt inclusions from a single Hawaiian volcano display δD values from -61 ± 4 ‰ to -165 ± 4 ‰ ([Hauri, 2002](#)). Whereas the heavier δD values (> -70 ‰) can be explained by a kinetic isotopic fractionation due to H diffusion from the melt inclusions, the most negative values (-103 ± 4 ‰ to -165 ± 4 ‰) negatively correlate with their water contents. This variation of δD values was modelled by the shallow open-system degassing of H_2O vapour with a vapour-melt hydrogen isotopic fractionation factor of 1.024 ([Hauri, 2002](#)). Thus, increased equilibrium degassing of H produces isotopically lighter silicate melts. This applies for the degassing of H as H_2O under present-day volcanic degassing conditions. Under more reduced conditions, such a lunar or martian magmatic degassing, H degasses as H_2 or CH_4 , producing isotopically heavier silicate melts as degassing increases ([Taylor *et al.*, 1986](#)).

Evidently, the degrees of such fractionations are expected to be smaller for C and S than for H due to the smaller relative mass differences between their isotopes. However, large C isotopic fractionations produced by C degassing have also been observed in degassed MORBs. For instance, $\delta^{13}\text{C}$ values range between -11.4 and -4.3 ‰ in MORBs from the South Indian Ridge and positively correlate with sample vesicularity, confirming the influence of degassing on C isotopic fractionation ([Cartigny *et al.*, 2001](#)). In melt inclusions from Koolau volcano, Hawaii, [Hauri \(2002\)](#) also observed large $\delta^{13}\text{C}$ variations (-12 to -21 ‰), again explained by C degassing. In both cases, these wide ranges of $\delta^{13}\text{C}$



values were explained by open-system (Rayleigh) rather than closed-system degassing. Yet, in the South Indian Ridge MORBs, the observed N isotopic fractionation during degassing is opposite to that of C isotopes, *i.e.* $\delta^{15}\text{N}$ values increase from -5.9 to $+2.1$ ‰ in the residual melt with increased degassing (Cartigny *et al.*, 2001). The opposite fractionation trends of C and N isotopes during degassing can be explained by their equilibrium degassing reactions. Carbon degasses as:



depending on whether it dissolves as carbonate or its more reduced form. Both degassing reactions produce a gas-melt isotopic fractionation factor >1 as determined by Javoy *et al.* (1976), and thus isotopically lighter silicate melts with increased C degassing. In contrast, in MORBs and OIBs, N is dissolved under its molecular form and degasses as:



which, as modelled in Figure 3, produces a gas-melt isotopic fractionation factor of 0.999, and thus isotopically heavier silicate melts with increased degassing. Under the more reduced conditions investigated in this study to simulate magma ocean degassing, this N degassing reaction no longer holds, as shown by Equations 4 and 5.

Sulfur degassing is more complex because sulfur is dissolved and degassed as multiple gaseous species depending on $f\text{O}_2$ conditions. Under reducing conditions comparable to those investigated herein, S dissolves into silicate melts as S^{2-} (Jugo *et al.*, 2010) and can degas as H_2S , COS , and S_2 in various proportions depending on pressure, temperature, and $f\text{O}_2$ conditions (Renggli *et al.*, 2017). Simplifying the issue by taking an average gas-melt sulfur isotopic fractionation factor of 1.003, Saal and Hauri (2021) successfully modelled the large variation of $\delta^{34}\text{S}$ values measured in lunar volcanic glasses ($+1.3$ to -14 ‰) as equilibrium open-system degassing. Therefore, increased degassing of sulfur under reduced conditions decreases the $\delta^{34}\text{S}$ values of silicate melts. However, at higher $f\text{O}_2$ conditions, S is dissolved as SO_4^{2-} in the silicate melt and degasses either as SO_2 or H_2S , and the $\delta^{34}\text{S}$ values of the silicate melt increase with increasing degassing (de Moor *et al.*, 2013).

Large kinetic nitrogen isotopic effects observed in natural mantle samples

Large variations have been observed among the nitrogen isotopic compositions of diverse mantle samples including diamonds (*e.g.*, Mikhail *et al.*, 2014) and xenoliths (Yokochi *et al.*, 2009; Banerjee *et al.* 2015; Yamamoto *et al.*, 2020). For instance, Yokochi *et al.* (2009) reported large isotopic disequilibria up to 25.4 ‰ between ferromagnesian minerals (olivine and pyroxene with positive $\delta^{15}\text{N}$ values) and phlogopite (with $\delta^{15}\text{N}$ as low as -17.3 ‰) in single peridotite xenoliths. Furthermore, both peridotitic and eclogitic diamonds show $\delta^{15}\text{N}$ values varying from <-40 ‰ to $>+20$ ‰ (Mikhail *et al.*, 2014). Whereas some of these variations can be explained by source variability, others cannot,



particularly $\delta^{15}\text{N}$ heterogeneities observed in single diamond samples (≤ 33 ‰; Mikhail *et al.*, 2014). Very interestingly, $\delta^{15}\text{N}$ variations in both xenoliths and diamonds are of the same order of magnitude as those measured in the degassed glasses from this study and are, therefore, too large to be explained by equilibrium N isotopic fractionations. Whereas Mikhail *et al.* (2014) could not conclude with certainty that kinetic isotopic fractionation was the only cause for the large range of $\delta^{15}\text{N}$ values they measured, Yokochi *et al.* (2009) presented evidence for kinetic isotopic fractionation during the substitution of NH_4^+ for N_2 in phlogopite during N uptake from the host magma. Therefore, as discussed in the main text, large kinetic N isotopic fractionations (≥ 25 ‰) resulting from a diffusive process at magmatic temperatures can be observed in natural settings and reproduced experimentally at high pressure and high temperature.

Supplementary Tables

Table S-1 Major element contents (wt. %) of silicate glasses; bdl, below detection limit.

Exp ID	SiO ₂	Al ₂ O ₃	FeO	MgO	CaO	Na ₂ O	K ₂ O	Total
<i>Fe-free degassed glasses</i>								
V152-PB05N	52.9 ± 0.3	7.8 ± 0.1	bdl	19.9 ± 0.3	6.8 ± 0.1	7.7 ± 0.1	3.4 ± 0.1	98.4 ± 0.3
V149-PB1N	52.5 ± 0.2	7.8 ± 0.2	bdl	20.5 ± 0.4	7.1 ± 0.1	7.2 ± 0.1	3.3 ± 0.1	98.3 ± 0.3
V129-PB2N	53.0 ± 0.2	7.9 ± 0.1	bdl	20.0 ± 0.4	6.7 ± 0.1	7.6 ± 0.1	3.5 ± 0.1	98.6 ± 0.4
V148-PB4N	54.2 ± 0.2	7.0 ± 0.1	bdl	21.3 ± 0.3	6.6 ± 0.2	7.2 ± 0.1	3.1 ± 0.1	99.3 ± 0.5
V133-PB4N2Si	57.9 ± 0.3	8.7 ± 0.1	bdl	17.0 ± 0.1	6.2 ± 0.1	7.6 ± 0.1	3.4 ± 0.1	100.8 ± 0.5
V125-PB8N	52.2 ± 0.2	7.4 ± 0.1	bdl	19.7 ± 0.2	6.6 ± 0.1	7.2 ± 0.1	3.1 ± 0.1	101.2 ± 0.2
V151-PB6N3Si	58.1 ± 0.4	6.3 ± 0.1	bdl	21.9 ± 0.3	5.5 ± 0.1	6.3 ± 0.1	2.6 ± 0.1	99.7 ± 0.3
V150-PB8N6Si	61.6 ± 0.6	5.7 ± 0.2	bdl	19.8 ± 0.6	6.0 ± 0.1	5.5 ± 0.1	2.6 ± 0.1	101.2 ± 0.4
<i>Fe-bearing glasses</i>								
V153-PBF05N	47.2 ± 0.3	8.3 ± 0.2	2.8 ± 0.1	19.6 ± 0.6	6.8 ± 0.1	7.5 ± 0.2	3.4 ± 0.1	95.7 ± 0.4
V142-PBF2N	50.2 ± 0.4	7.7 ± 0.1	4.5 ± 0.1	18.4 ± 0.2	7.1 ± 0.1	7.3 ± 0.1	3.4 ± 0.1	98.7 ± 0.4
V141-PBF4N	50.9 ± 0.3	8.0 ± 0.1	2.0 ± 0.1	18.6 ± 0.3	7.5 ± 0.1	6.5 ± 0.1	3.3 ± 0.1	96.7 ± 0.4
V145-PBF4N2Si	53.4 ± 0.2	7.2 ± 0.1	1.8 ± 0.1	19.6 ± 0.4	6.4 ± 0.1	6.5 ± 0.1	3.2 ± 0.1	98.1 ± 0.5
V147-PBF8N	54.9 ± 0.4	7.0 ± 0.2	0.9 ± 0.1	20.2 ± 0.4	6.2 ± 0.1	7.0 ± 0.2	3.2 ± 0.1	99.3 ± 0.4
V154-PBF6N3Si	58.0 ± 0.5	6.9 ± 0.1	0.8 ± 0.4	19.4 ± 0.3	5.9 ± 0.1	6.3 ± 0.1	3.0 ± 0.1	100.3 ± 0.5
V155-PBF8N6Si	62.8 ± 0.5	5.9 ± 0.2	0.2 ± 0.2	19.6 ± 0.3	5.0 ± 0.1	5.5 ± 0.1	2.7 ± 0.1	101.6 ± 0.7



Table S-2 Fe, Pt, and Si contents (wt. %) of metal blobs and estimated fO_2 conditions.

Exp ID	Fe	Pt	Si	fO_2 (IW)
V141- PBF4N	92.0 ± 0.3	0.03 ± 0.03	0.04 ± 0.02	−2.3
V145-PBF4N2Si	94.0 ± 0.2	0.16 ± 0.04	0.007 ± 0.004	−2.6
V147-PBF8N	94.2 ± 0.4	0.30 ± 0.06	0.04 ± 0.01	−3.3
V154-PBF6N3Si	92.9 ± 0.3	0.4 ± 0.2	0.007 ± 0.002	−3.4
V155-PBF8N6Si	77.1 ± 0.9	1.8 ± 1.8	20.9 ± 1.1	−4.2

Supplementary Figures

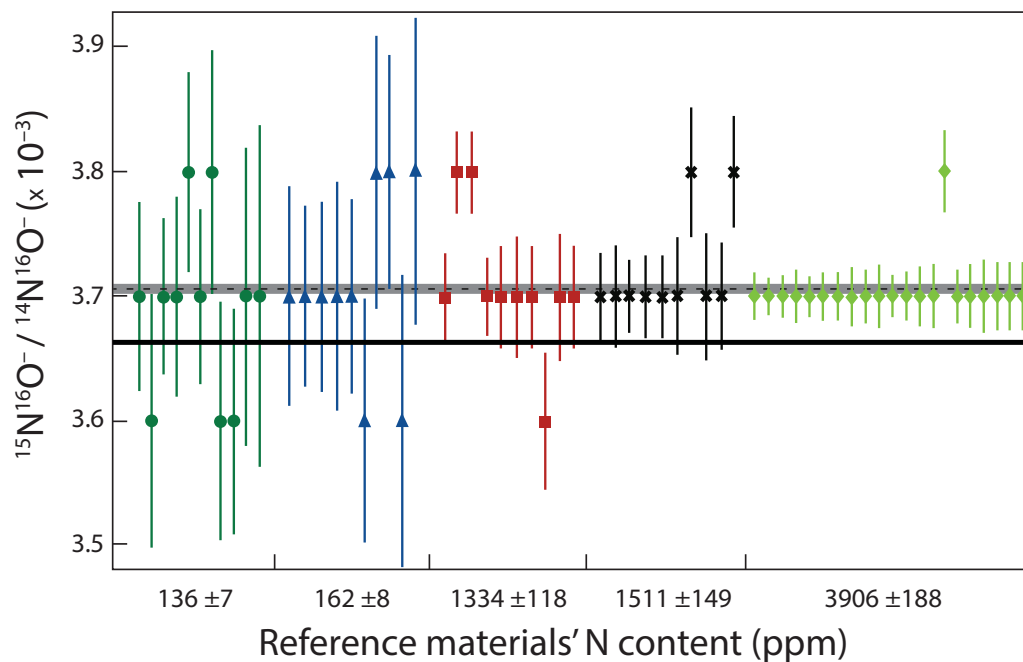


Figure S-1 Measured $^{15}N^{16}O^- / ^{14}N^{16}O^-$ ratios in five reference glasses used to calculate IMF. Each symbol corresponds to a reference glass whose N content was previously measured by static mass spectrometry (Füri *et al.*, 2018). The dashed line is the average of all standard analyses calculated using IsoplotR (Vermeesch, 2018) with 2σ uncertainties (shown by the grey shaded bar). The true $^{15}N/^{14}N$ value of these reference glasses is shown by the black line (~ 0.003662). The ratio of the average to the true value (*i.e.* the dashed and solid lines, respectively) is α_{inst} .

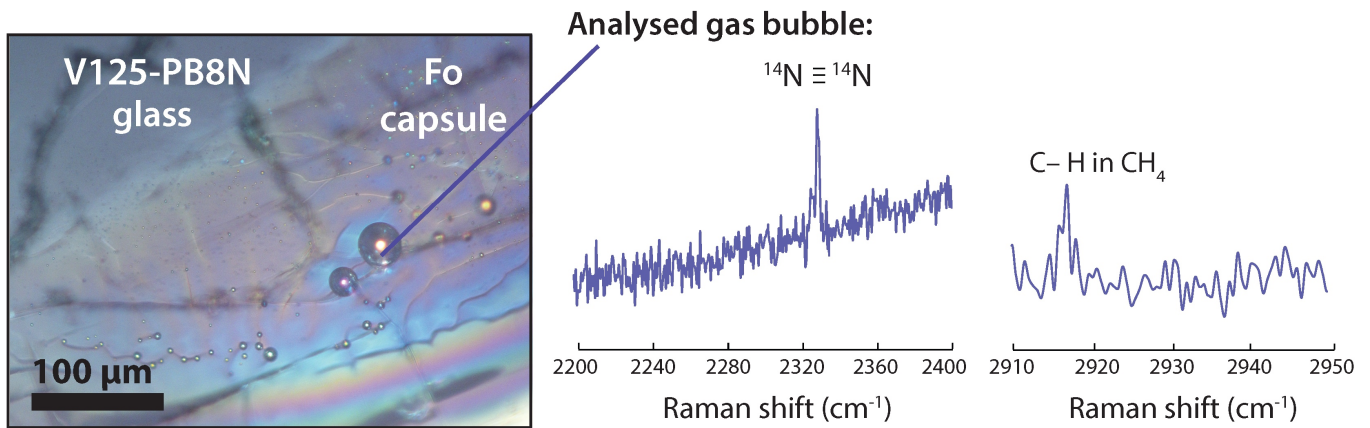


Figure S-2 Raman spectra obtained in bubbles of sample V125-PB8N.

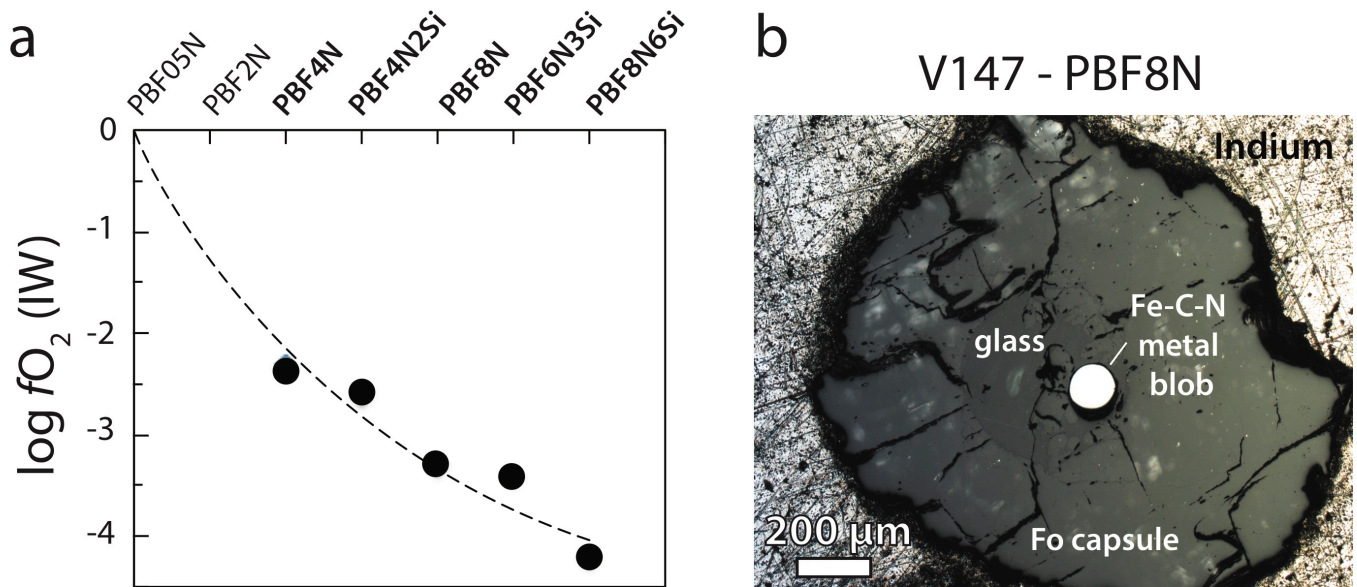


Figure S-3 (a) fO_2 conditions (relative to the IW buffer) calculated for samples containing sufficiently large metal blobs (b). The fO_2 conditions of samples in which metal blobs were too small to be analysed ($<5 \mu\text{m}$) were estimated by extrapolation of the trend, *i.e.*, $\log fO_2$ as a function of the amount of reducing agent (Si_3N_4 and Si metal) added (dashed line, log function).

Supplementary Information References

Aubaud, C., Pineau, F., Hékinian, R., Javoy, M. (2006) Carbon and hydrogen isotope constraints on degassing of CO_2 and H_2O in submarine lavas from the Pitcairn hotspot (South Pacific). *Geophysical Research Letters* 33, L02308.

Bernadou, F., Gaillard, F., Füre, E., Marrocchi, Y., Slodczyk, A. (2021) Nitrogen solubility in basaltic silicate melt—Implications for degassing processes. *Chemical Geology* 573, 120192.

Banerjee, S., Kyser, T.K., Mitchell, R. (2015) Nitrogen isotopic compositions and concentrations in MARID xenoliths. *Chemical Geology* 391, 83–89.

- Boulliung, J., Füre, E., Dalou, C., Tissandier, L., Zimmermann, L., Marrocchi, Y. (2020) Oxygen fugacity and melt composition controls on nitrogen solubility in silicate melts. *Geochimica et Cosmochimica Acta* 284, 120-133.
- Cartigny, P., Harris, J.W., Javoy, M. (2001) Diamond genesis, mantle fractionations and mantle nitrogen content: a study of $\delta^{13}\text{C}$ -N concentrations in diamonds. *Earth and Planetary Science Letters* 185, 85-98.
- Dalou, C., Hirschmann, M.M., von der Handt, A., Mosenfelder, J., Armstrong, L.S. (2017) Nitrogen and carbon fractionation during core-mantle differentiation at shallow depth. *Earth and Planetary Science Letters* 458, 141-151.
- Dalou, C., Füre, E., Deligny, C., Piani, L., Caumon, M.C., Laumonier, M., Boulliung, B., Edén, M. (2019) Redox control on nitrogen isotope fractionation during planetary core formation. *Proceedings of the National Academy of Sciences* 116, 14485-14494.
- De Hoog, J.C., Taylor, B.E., Van Bergen, M.J. (2009) Hydrogen-isotope systematics in degassing basaltic magma and application to Indonesian arc basalts. *Chemical Geology* 266, 256-266.
- de Moor, J.M., Fischer, T.P., Sharp, Z.D., King, P.L., Wilke, M., Botcharnikov, R.E., Cottrell, E., Zelenski, M., Marty, B., Klimm, K., Rivard, C., Ayalew, D., Ramirez, C., Kelley, K.A. (2013) Sulfur degassing at Erta Ale (Ethiopia) and Masaya (Nicaragua) volcanoes: Implications for degassing processes and oxygen fugacities of basaltic systems. *Geochemistry, Geophysics, Geosystems* 14, 4076-4108.
- Fichtner, C.E., Schmidt, M.W., Liebske, C., Bouvier, A.S., Baumgartner, L.P. (2021) Carbon partitioning between metal and silicate melts during Earth accretion. *Earth and Planetary Science Letters* 554, 116659.
- Füre, E., Deloule, E., Dalou, C. (2018) Nitrogen abundance and isotope analysis of silicate glasses by secondary ionization mass spectrometry. *Chemical Geology* 493, 327-337.
- Hauri, E. (2002) SIMS analysis of volatiles in silicate glasses, 2: isotopes and abundances in Hawaiian melt inclusions. *Chemical Geology* 183, 115-141.
- Hirschmann, M.M., Withers, A.C., Ardia, P., Foley, N.T. (2012) Solubility of molecular hydrogen in silicate melts and consequences for volatile evolution of terrestrial planets. *Earth and Planetary Science Letters* 345, 38-48.
- Gerlach, T.M., Taylor, B.E. (1990) Carbon isotope constraints on degassing of carbon dioxide from Kilauea Volcano. *Geochimica et Cosmochimica Acta* 54, 2051-2058.
- Grewal, D.S., Dasgupta, R., Holmes, A.K., Costin, G., Li, Y., Tsuno, K. (2019) The fate of nitrogen during core-mantle separation on Earth. *Geochimica et Cosmochimica Acta* 251, 87-115.
- Iacono-Marziano, G., Morizet, Y., Le Trong, E., Gaillard, F. (2012) New experimental data and semi-empirical parameterization of H_2O - CO_2 solubility in mafic melts. *Geochimica et Cosmochimica Acta* 97, 1-23.
- Javoy, M., Pineau, F., Iiyama, I. (1978) Experimental determination of the isotopic fractionation between gaseous CO_2 and carbon dissolved in tholeiitic magma. *Contributions to Mineralogy and Petrology* 67, 35-39.
- Jugo, P.J., Wilke, M., Botcharnikov, R.E. (2010) Sulfur K-edge XANES analysis of natural and synthetic basaltic glasses: Implications for S speciation and S content as function of oxygen fugacity. *Geochimica et Cosmochimica Acta* 74, 5926-5938.
- Médard, E., McCammon, C.A., Barr, J.A., Grove, T.L. (2008) Oxygen fugacity, temperature reproducibility, and H_2O contents of nominally anhydrous piston-cylinder experiments using graphite capsules. *American Mineralogist* 93, 1838-1844.
- Mikhail, S., Verchovsky, A.B., Howell, D., Hutchison, M.T., Southworth, R., Thomson, A.R., Warbuton, A.P., Jones, A.P., Milledge, H.J. (2014) Constraining the internal variability of the stable isotopes of carbon and nitrogen within mantle diamonds. *Chemical Geology* 366, 14-23.
- Pineau, F., Javoy, M. (1994) Strong degassing at ridge crests: The behaviour of dissolved carbon and water in basalt glasses at 14 N, Mid-Atlantic Ridge. *Earth and Planetary Science Letters* 123, 179-198.
- Renggli, C.J., King, P.L., Henley, R.W., Norman, M.D. (2017) Volcanic gas composition, metal dispersion and deposition during explosive volcanic eruptions on the Moon. *Geochimica et Cosmochimica Acta* 206, 296-311.
- Saal, A.E., Hauri, E.H. (2021) Large sulfur isotope fractionation in lunar volcanic glasses reveals the magmatic differentiation and degassing of the Moon. *Science Advances* 7, eabe4641.



- Shishkina, T.A., Botcharnikov, R.E., Holtz, F., Almeev, R.R., Portnyagin, M.V. (2010) Solubility of H₂O- and CO₂-bearing fluids in tholeiitic basalts at pressures up to 500 MPa. *Chemical Geology* 277, 115-125.
- Speelmanns, I.M., Schmidt, M.W., Liebske, C. (2019) The almost lithophile character of nitrogen during core formation. *Earth and Planetary Science Letters* 510, 186-197.
- Stanley, B.D., Hirschmann, M.M., Withers, A.C. (2014) Solubility of C-O-H volatiles in graphite-saturated martian basalts. *Geochimica et Cosmochimica Acta* 129, 54-76.
- Taylor, B.E. (1986) Magmatic volatiles: isotopic variation of C, H, and S. In: Valley, J.W., Taylor, H.P., O'Neil, J.R. (Eds.) *Stable isotopes in high temperature geological processes. Reviews in Mineralogy and Geochemistry* 16, 185-226.
- Vermeesch, P. (2018) IsoplotR: A free and open toolbox for geochronology. *Geoscience Frontiers* 9, 1479-1493.
- Wade, J., Wood B.J. (2005) Core formation and the oxidation state of the Earth. *Earth and Planetary Science Letters* 236, 78-95.
- Yamamoto, J., Takahata, N., Sano, Y., Yanagita, M., Arai, S., Prikhod'ko, V.S. (2020) Nitrogen and noble gas isotopic compositions of mantle xenoliths from Far Eastern Russia: Implications for nitrogen isotopic characteristics of mantle wedge fluid. *Earth and Planetary Science Letters* 534, 116109.
- Yokochi, R., Marty, B., Chazot, G., Burnard, P. (2009) Nitrogen in peridotite xenoliths: Lithophile behavior and magmatic isotope fractionation. *Geochimica et Cosmochimica Acta* 73, 4843-4861.
- Zhang, C., Duan, Z. (2009) A model for C–O–H fluid in the Earth's mantle. *Geochimica et Cosmochimica Acta* 73, 2089-2102.
- Zhang, H.L., Hirschmann, M.M., Cottrell, E., Newville, M., Lanzirotti, A. (2016) Structural environment of iron and accurate determination of Fe³⁺/ΣFe ratios in andesitic glasses by XANES and Mössbauer spectroscopy. *Chemical Geology* 428, 48-58.

